

1 *FTICR Mass spectrometry imaging at extreme mass resolving power using*  
2 *a dynamically harmonized ICR cell with 1 $\omega$  or 2 $\omega$  detection*

3 Mathieu Tiquet<sup>1</sup>, Raphaël La Rocca<sup>1</sup>, Stefan Kimbauer<sup>2</sup>, Samuele Zoratto<sup>2</sup>, Daan van Kruining<sup>3</sup>, Loïc  
4 Quinton<sup>1</sup>, Gauthier Epe<sup>1</sup>, Pilar Martinez-Martinez<sup>3</sup>, Martina Marchetti-Deschmann<sup>2</sup>, Edwin De Pauw<sup>1</sup>,  
5 Johann Far<sup>1</sup>

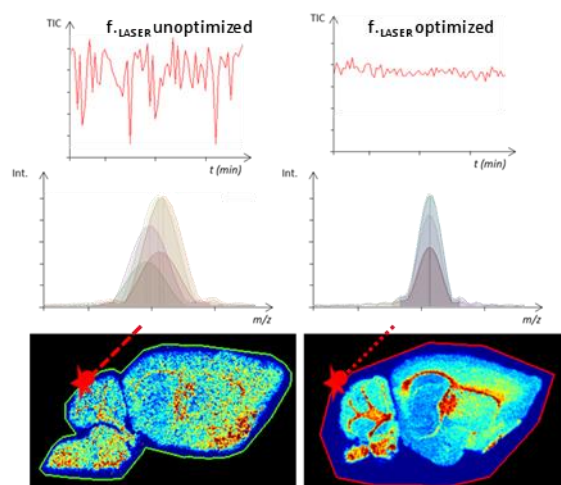
6  
7 <sup>1</sup> Mass Spectrometry Laboratory, MolSys Research Unit, University of Liège; Quartier Agora, Liège,  
8 Belgium

9 <sup>2</sup> Institute of Chemical Technologies and Analytics, TU Wien (Vienna University of Technology), Vienna,  
10 Austria

11 <sup>3</sup> Department of Psychiatry and Neuropsychology, School for Mental Health and Neuroscience,  
12 Maastricht University, Maastricht, the Netherlands

13 **Abstract**

14 *MALDI mass spectrometry imaging (MALDI MSI) is a*  
15 *powerful analytical method providing the 2D*  
16 *localization of compounds from thin sections of*  
17 *typically but not exclusively biological samples. The*  
18 *dynamically harmonized ICR cell (ParaCell©) was*  
19 *recently introduced to achieve extreme spectral*  
20 *resolution capable to provide the isotopic fine*  
21 *structure of ions detected in complex samples. The*  
22 *latest improvement in ICR technology also includes*  
23 *2 $\omega$  detection which significantly reduces the transient*  
24 *time while preserving the nominal mass resolving*



25 *power of the ICR cell. High-resolution MS images acquired on FT-ICR instruments equipped with 7T*  
26 *and 9.4T superconducting magnets and the dynamically harmonized ICR cell operating at suboptimal*  
27 *parameters, suffered severely from the pixel-to-pixel shifting of m/z peaks due to space-charge effects.*  
28 *The resulting profile average mass spectra have depreciated mass measurement accuracy and mass*  
29 *resolving power under the instrument specifications that affect the confidence level of the identified*  
30 *ions. Here we propose an analytical workflow based on the monitoring of the Total Ion Current to restrain*  
31 *the pixel-to-pixel m/z shift. Adjustment of the laser parameters is proposed to maintain high spectral*  
32 *resolution and mass accuracy measurement within the instrument specifications during MSI analyses.*  
33 *The optimized method has been successfully employed in replicates to perform high-quality MALDI MS*  
34 *images at resolving power (FWHM) above 1,000,000 in the lipid mass range across the whole image*  
35 *for superconducting magnets of 7T and 9.4T using 1 and 2 $\omega$  detection. Our data also compare favorably*  
36 *with MALDI MSI experiments performed on higher magnetic field superconducting magnets, including*  
37 *the 21T MALDI FT-ICR prototype instrument of the NHMFL group at Tallahassee, Florida.*

38

39

## 40 1. Introduction

41 Matrix-Assisted Laser Desorption/Ionization Mass Spectrometry Imaging (MALDI-MSI) has emerged  
42 as a label-free analytical method monitoring the relative abundance (despite severe limitations due to  
43 suppression effects) and spatial distribution for a wide variety of analytes, especially for biological  
44 samples<sup>1-3</sup>. To properly distinguish isobaric compounds<sup>4</sup> inherent to the complexity of biological  
45 samples, high resolving powers at full width at half maximum ( $R.P._{FWHM} > 300,000$  at  $400 m/z$ ) and a  
46 reliable mass measurement accuracy (MMA) are required in the absence of an upstream separation  
47 method (such as ion mobility). These performances are commonly achieved by Fourier Transform mass  
48 analyzer such as Fourier Transform-Ion Cyclotron Resonance (FT-ICR)<sup>5</sup>. The Bruker dual ion source  
49 ESI/MALDI FT-ICR (solariX and scimaX) is a hybrid instrument equipped with multipoles, a quadrupole,  
50 and a collision cell for precursor ion selection and fragmentation. Ions produced by electrospray (ESI)  
51 and MALDI are also accumulated in the multipole region to prepare the ion packet to be introduced into  
52 the ICR cell. Consequently, almost any combination of MALDI laser settings are compatible with any  
53 transient time for mass spectra acquisition. Recent developments introduced by E.N. Nikolaev *et al.*<sup>6-8</sup>  
54 led to the dynamically harmonized ICR cell commercialized by Bruker in the solariX XR and scimaX XR  
55 brand FT-ICR mass spectrometers under the name ParaCell®. This new cell offers the highest mass  
56 resolving power (R.P.) currently achievable for such instruments<sup>9</sup> (around 1,000,000 in the lipid mass  
57 range in broadband mode) and mass measurement accuracy typically is in the sub-ppm range. These  
58 improvements drastically increase the confidence level of the precursor ions empiric formula  
59 determination, especially when including the fine isotopic structure<sup>10</sup>. Moreover, the introduction<sup>11-13</sup>  
60 and the experimental application<sup>12,14</sup> of  $2\omega$  detection drastically improved the mass R.P. and the scan  
61 duration of the ICR transient signals.

62 To obtain the highest quality of mass spectrometry images (MSI) in terms of mass R.P. and lateral  
63 resolution, each step of the imaging workflow has to be properly optimized. The experimental  
64 optimization of the FT-ICR-MS(I) instrument<sup>15</sup> was studied by Carlos Afonso and Abdellah Tebani's  
65 group. The sample preparation affects the ionization efficiency as well as the local diffusion of the  
66 analytes in tissue sections. Different experimental parameters were evaluated extensively in the  
67 literature including slice thickness<sup>16-18</sup>, matrix and solvent selection<sup>19-23</sup>, and optimization of the  
68 automatized matrix deposition<sup>24</sup>. When using the recommended parameters and optimized methods  
69 intended for the previous ICR design, the "Infinity Cell®", the best performance in terms of  $R.P._{FWHM}$

70 and mass accuracy was far from instrument specifications due to abnormally large mass shifts. From  
71 an instrumental point of view, significant deviations of the amount of injected ions between scan events  
72 heavily affect the global performance of the Paracell. Pixel-to-pixel fluctuations of the ion current during  
73 the MSI experiments cause a non-repeatable space charge effect between pixels in regards to the  
74 MALDI-MS calibration procedure. In general, this phenomenon can be corrected using a lock-mass  
75 calibration during acquisition<sup>25,26</sup> which would ideally require several homogeneously distributed  
76 analytes. These targets could be added before matrix deposition at the risk of inducing more or less  
77 severe ion suppression effect(s) and lateral diffusion. An alternative is to use post-acquisition  
78 recalibration software<sup>27</sup>, which however can be time-consuming due to format conversion and  
79 computational steps depending on the size and format of the dataset.

80 This study reports optimized instrument conditions to mitigate the abnormal mass shifts observed  
81 during high/extreme resolution MALDI FT-ICR MSI fitted with the ParaCell®. We present here such an  
82 optimization on sample preparation and acquisition parameters to produce MS images at R.P.<sub>FWHM</sub> at  
83 least better than 500,000 at  $m/z$  800 (better than 1 million at  $m/z$  400) in broadband mode using a  
84 solariX XR 9.4T and a scimaX 7T 2XR.

## 85 **2. Material and methods**

### 86 **2.1. Chemicals**

87 Acetone and methanol HPLC grade were obtained from Biosolve (Valkenswaard, Netherlands).  
88 Trifluoroacetic acid (TFA, 99%)  $\alpha$ -cyano-4-hydroxycinnamic acid ( $\alpha$ -HCCA, purity 97%), and red  
89 phosphorus (>97%) were purchased from Sigma-Aldrich (Taufkirchen, Germany). The internal standard  
90 SPLASH LipidoMIX™ containing deuterated lipids from different families was purchased from Avanti  
91 Polar Lipids (Alabaster, Alabama, USA) via Sigma Aldrich.

### 92 **2.2. Animal handling**

93 Transgenic mice were purchased from Dr. Mary Jo LaDu (University of Illinois at Chicago) and bred  
94 in-house at MHeNs at Maastricht University as described elsewhere<sup>28</sup>. In short, human-APOE4 knock-  
95 in mice in which the mouse APOE gene was replaced by human APOE were crossbred with 5xFAD  
96 mice (Jackson laboratory) carrying human familial Alzheimer disease mutations PSEN1 and APP to  
97 obtain E4FAD mice with increased A $\beta$  peptide production<sup>28,29</sup>. Female E4FAD mice over 6 months of  
98 age were sacrificed by CO<sub>2</sub> inhalation then brains were extracted. Mice brains were cut across the  
99 sagittal midline and immediately fresh-frozen in liquid nitrogen and subsequently stored at -80 °C. For

100 transportation, samples were placed on dry ice and transferred to the University of Liège to be long-  
101 term stored conserved again at -80°C before further handling. All procedures were approved by the  
102 Animal Welfare Committee of Maastricht University (n° AVD107002015177) and were performed  
103 according to Dutch federal regulations for animal protection.

104 Natural AB-type zebrafish were bred by the Groupement Interdisciplinaire de Génoprotéomique  
105 Appliquée (GIGA) at ULiège under the supervision of Pr. Marc Muller. The aquarium water was  
106 thermostated at 28°C with a circadian cycle of 14 hours of light and 10 hours of darkness. One-month-  
107 old fish were first anesthetized by adding tricaine mesylate to a concentration of 0.04% then increased  
108 to 0.16% to induce cardiac arrest. Fish were then embedded in gelatin (350mg.mL<sup>-1</sup>) and stored at -  
109 80°C for at least 24 hours. All procedures were approved by the Animal Welfare Committee of the  
110 University of Liège (n° 20-2284) and were performed according to Belgian federal regulations for animal  
111 protection.

### 112 **2.3. Tissue sectioning**

113 Sectioning was performed on a CryoStar NX70 (Thermo Fisher Scientific, Massachusetts, USA) set  
114 at -20°C. SEC35e low profile razor blades (Thermo Fisher Scientific, Massachusetts, USA) were  
115 employed at -15°C during the sectioning. Mouse brain and zebrafish whole-body sagittal slices were  
116 sectioned at a medium thickness of 14 µm and 8 µm to keep a good amount of material for ionization<sup>30</sup>  
117 while easing the collection of seriated slices. Cryosections were thaw-mounted onto indium-tin-oxide  
118 (ITO) coated conductive glass slides (Bruker Daltonics, Bremen, Germany).

### 119 **2.4. Matrix coating**

120 Prior to matrix deposition, samples were dried in a vacuum desiccator for 15 minutes or until no  
121 visible wetness was observable. Dried samples were coated with matrix using the automatic sprayer  
122 SunCollect MALDI spotter (SunChrom, Friedrichsdorf, Germany). Matrix solution contained 5mg.mL<sup>-1</sup>  
123 of α-HCCA dissolved in methanol and milli-Q water acidified with TriFluoroacetic Acid (MeOH:H<sub>2</sub>O:TFA  
124 9:0.99:0.01 v:v:v). During the spraying procedure, the nozzle was positioned to its lowest setting and  
125 its moving speeds in the X and Y axis were set at medium 10 (1540 mm.min<sup>-1</sup>). Matrix flow rates started  
126 from 5µL.min<sup>-1</sup> up to the 4<sup>th</sup> layer for which flow rates were increased to 10µL.min<sup>-1</sup> until the last  
127 deposition layer. The number of layers required to obtain a homogenous coating of roughly 10nmol.mm<sup>-2</sup>  
128 of matrix was calculated for each spray deposition. The amount of matrix sprayed is confirmed by  
129 weight comparison of the ITO glass slide before and after the spray process. Later in this study, the

130 optimized amount of deposited matrix is 5nmol.mm<sup>-2</sup>.

## 131 2.5. MALDI mass spectrometry imaging

132 Mass spectrometry acquisitions were performed on ESI/MALDI dual-source MALDI FT-ICRs  
133 equipped with the ParaCell® (solariX XR 9.4T and scimaX 2XR 7T, Bruker Daltonics, Bremen,  
134 Germany) operating in MALDI positive mode with a data point size of 2, 4, and 8M, or 16M for the  
135 scimaX 2XR in the 300 to 1200 *m/z* mass range using the Amplitude mode. Other relevant parameters  
136 for the solariX XR 9.4T and the scimaX 7T 2XR are listed in Table 1. The shimming of the ICR cells  
137 was performed using the recommended procedure by the manufacturer based on the infusion of sodium  
138 trifluoroacetic solution in 50% acetonitrile. Before *m/z* calibration, the tissue to be analyzed, or a seriated  
139 tissue test section, was first probed to determine the minimum required laser power and monitor the ion  
140 current to set the laser parameters. Then, the *m/z* calibration of the spectrometer was performed using  
141 the odd-numbered clusters of red phosphorus spotted close to the analyzed samples<sup>31</sup>. During  
142 calibration, a TIC as close as possible to the value obtained on tissue was targeted with the help of  
143 selective accumulation upper and lower cutoff set at maximum  $\pm 20\%$  of the probed TIC on the sample.  
144 In our case, the laser powers of the solariX XR and the scimaX 2XR were adjusted from 10 to 16%  
145 depending on the number of ions to be injected in the ICR cell. The laser power could be higher  
146 depending on the rate of wear of the laser. Typical high vacuum values of the ICR cells were about  
147  $2.5 \times 10^{-10}$  mbar and the targeted TIC with a data size of 4M was  $5 \times 10^8$  cps.

148 Automated acquisitions were performed using the software FlexImaging 5.0 (Bruker Daltonics,  
149 Bremen, Germany) with a raster of 50 $\mu$ m in both (x,y) axes.

150 **Table 1 Sets of parameters used in the original and re-optimized method. The laser power was**  
151 **adjusted to get the lower power possible when the TIC signal was reaching  $5 \times 10^8$  cps. Values**  
152 **in brackets show a working range.**

Parameters	(Unit)	solariX XR		scimaX 2XR 1 or 2 $\omega$	
		Original	Re-optimized	Original	Re-optimized
Laser focus <sup>a</sup>	%	98	80	93	85
Laser shots	(#shots)	600	[2 ; 10]	400	6
Laser frequency	(Hz)	1000	#shots $\times 10$	1000	60
Sweep excitation power	(%)	22	[16 ; 18]	20	18
Front & back trap plate	(V)	1.5	1.35	3	3.06
Analyzer entrance	(V)	-10	-10	-10	-10
Side Kick	(V)	5	[6 ; 10]	0.2	3
Side Kick Offset	(V)	-1.0	-1.5	-1.5	-1.5
Time of flight	(ms)	1.2	1.2	1.0	0.7 <sup>b</sup>

153 <sup>a</sup> small and medium laser focus for solariX XR and the scimaX 2XR, respectively

154 <sup>b</sup> time of flight set at 0,7ms for the 2 $\omega$  acquisition for 16M data point only

155

## 156 2.6. Data processing

157 All datasets were visualized with SCiLS Lab 2016b (SCiLS, Bremen, Germany) after conversion into  
158 scilslab format using the SQLite file generated by the instrument. MALDI-MSI were generated after total  
159 ion count normalization (unless specified otherwise) and automatic hot spot removal (at 99% quantile).  
160 Database bulk structure searches were performed using the LIPID MAPS Structure Database (LMSD)  
161 tool offered by LIPID MAPS® Lipidomics Gateway (lipidmaps.org)<sup>32,33</sup>. Queries were submitted on the  
162 full database with a 5mDa mass tolerance for [M+H]<sup>+</sup>, [M+H-H<sub>2</sub>O]<sup>+</sup>, [M+Na]<sup>+</sup>, [M+K]<sup>+</sup>, and [M+2Na-H]<sup>+</sup>  
163 ions. The nomenclature of lipids used in this work is based on the recommended lipids classification by  
164 Fahy and coworkers<sup>34</sup>. An in-house script written in R language has been used to calculate the standard  
165 deviation for MMA and R.P. for a given *m/z* window within an MSI dataset converted to imzML format  
166 by FlexImaging 5.0.

## 167 3. Results and discussion

168 Most of the published work reporting the optimization of MALDI FT-ICR MSI methods was performed  
169 on instruments fitted with superconducting magnets of 12T and 15T or above. We propose here to visit  
170 or revisit the influence of the instrument parameters to produce MALDI images with the highest possible  
171 mass R.P. and MMA that such instruments can offer on most readily available commercial FT-ICR  
172 instruments equipped with a 7 or 9.4T magnet.

173 A higher magnetic field limits the space-charge effects inside the ICR cell and provides improved  
174 tolerance in regards to the number of injected ions. During MALDI MSI experiments, the amount of  
175 injected ion significantly varies due to the intrinsic heterogeneity of the biological material in terms of  
176 molecular composition and dynamic range of the acquisition method. Consequently, instruments using  
177 lower magnetic fields could be substantially affected by impaired performance. The analytical workflow,  
178 from matrix deposition to ion optics parameters, was investigated and applied to MALDI FT-ICR  
179 instruments using 7T (scimaX 2XR) or 9.4T (solariX XR) superconducting magnets and the 1 $\omega$  or 2 $\omega$   
180 detection mode, when available. Additionally, ion source parameters, only poorly explored in the  
181 literature, were explored at optimal settings to improve the quality of MALDI images at very high mass  
182 R.P.

183 **3.1. Magnetic field and charge-space effects.** The determination of the *m/z* ratios by FT-ICR is  
184 obtained by converting the rotational frequencies of the ions by Fourier Transformation, which depends

185 on the masses and carried charges under the influence of the applied magnetic fields. The space-  
 186 charge effect limits the performance of an FT-ICR due to the influence of the charge repulsion between  
 187 ion packets if the ICR cell is loaded with more ions than the magnetic field can constrain. Using a  
 188 superconductive magnet with higher magnetic fields would limit this influence as explained by in  $\omega_{obs} =$   
 189  $\frac{qB}{m} - \frac{2\alpha V}{a^2 B} - \frac{q\rho G_i}{\epsilon_0 B}$  Equation 1, where the unperturbed ion frequency  $\omega_{obs}$  is the observed  
 190 frequency (which is then converted into a signal in the mass spectrum) equaling the unperturbed  
 191 cyclotron frequency minus the magnetron frequency for an ion in a perfectly quadrupolar static field  
 192 minus the space-charge component of the mass shift<sup>35,36</sup>. In Equation 1,  $q$  represents the ion charge,  
 193  $B$  the magnetic field strength,  $m$  the ion mass,  $\alpha$  the separation between the trapping plates,  $V$  the  
 194 voltage difference between upper and side plates,  $a$  the separation between upper and lower plates,  $\rho$   
 195 the ion density,  $G_i$  the ion cloud geometry and  $\epsilon_0$  the void permittivity constant.

$$196 \quad \omega_{obs} = \frac{qB}{m} - \frac{2\alpha V}{a^2 B} - \frac{q\rho G_i}{\epsilon_0 B} \quad \text{Equation 1}$$

197 In the third term, the importance of ion density and cloud geometry describes the impact of the  
 198 number of injected ions on the angular velocity  $\omega$  and consequently, the mass shift observed in the  
 199 mass spectra. The influence of the magnetic field also restrains the mass shift to some extent (only in  
 200 the denominator). In this paper, the main focus is on limiting the ion current fluctuation during the MSI  
 201 acquisition and restricting the observed mass shift to the extent possible. This corresponds to limiting  
 202 the fluctuations of the space-charge effect components at a constant magnetic field. Nonetheless, the  
 203 requirement for the magnetic field to produce MALDI images at extreme mass R.P. was evaluated by  
 204 comparing experimental results from 9.4T to a 7T operated in  $1\omega$  and/or  $2\omega$  detection modes.

205 Considering theory, the best chance to restrain the experimental mass shift in the average MS  
 206 images under the specification of the FT-ICR is to prevent space-charge effects. This was investigated  
 207 by experimental work and a literature survey for the different steps of the production of MALDI images,  
 208 from sample preparation (matrix deposition protocols) to instrumental parameters (ion optics  
 209 transmission, ICR ion optics). Furthermore, optimization works for laser adjustments are still scarce in  
 210 the literature and were also investigated.

211 The monitored outputs of experimental parameters during measurement at very high mass R.P.  
 212 (500,000 and above in the lipid mass range) were mainly the stability of the total ion current (TIC)  
 213 fluctuation, the mass shift (i.e. pixel-to-pixel variation of the  $m/z$  peak apexes) and the mass R.P. (R.P.

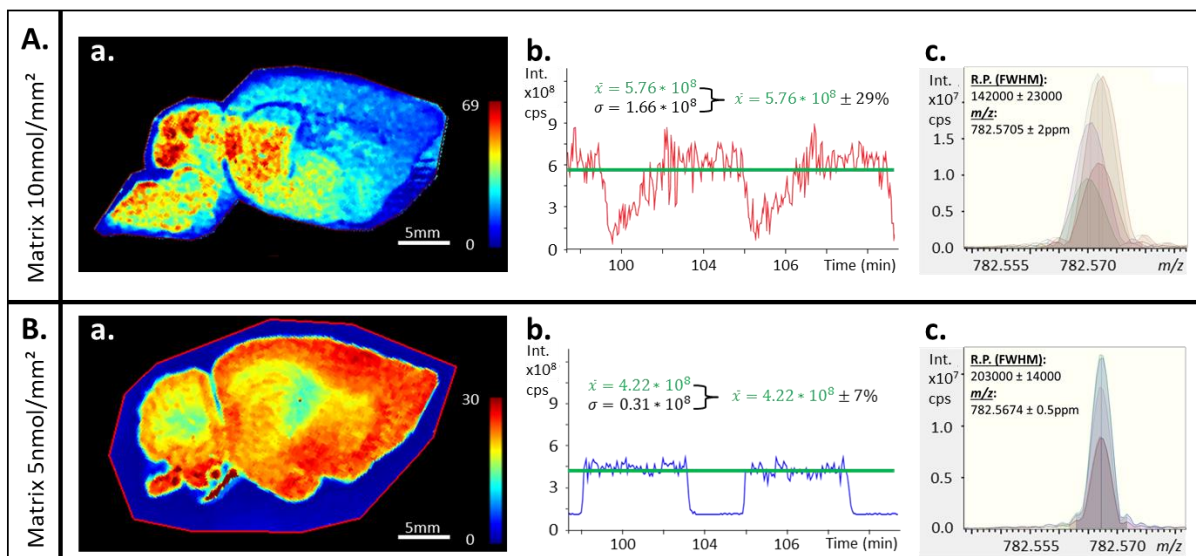
214 expressed as full width at half maximum, FWHM) for the individual pixel and in the profile average mass  
215 spectrum of the image. The apparent intra-scan dynamic range between major and minor peaks of  
216 lipids was also monitored and reported during the laser parameter optimization.

217 The effect of significant TIC fluctuations on the  $m/z$  shift was evaluated by monitoring the signal  
218 produced by a standard Splash LipidomiX solution of deuterated lipids spotted with  $\alpha$ -HCCA matrix on  
219 an ITO glass slide. After the acquisition of a single MALDI-MS scan involving 10 laser shots, the  
220 instrument was post-calibrated using the signals from [PC (15:0/18:1(d7))+H]<sup>+</sup>  $m/z$  753.613, [LysoPC  
221 (18:1(d7))+H]<sup>+</sup>  $m/z$  529.399 and [SM (d18:1/18:1(d9))+H]<sup>+</sup>  $m/z$  738.647. The acquired signal was  
222 observed with an R.P. above 200,000 (FWHM) at their respective  $m/z$  and MMA better than 0.5ppm  
223 (MMA after post-calibration). When the number of injected ions was increased (i.e. using 400 laser  
224 shots), it resulted in a 10x higher total ion count injected into the ICR cell and a mass shift for all  
225 experimentally observed  $m/z$  values resulting in an MMA between 2 and 8 ppm. The larger amount of  
226 ions introduced into the cell in regards to the calibration procedure severely impaired the MMA. An  
227 abrupt modification of the TIC intentionally generated by suddenly increasing the number of laser shots  
228 was correlated with the observed mass shift. An example is provided in Figure S1 for illustration based  
229 on the signal obtained for [PC (15:0/18:1(d7))+H]<sup>+</sup>.

230 From an MSI perspective, such TIC variations commonly appear when inhomogeneous matrix  
231 deposition creates hot spots, and/or when samples, such as tissue sections, have intrinsically  
232 heterogeneous regions in terms of molecular compositions and/or desorbed/ionized efficiencies.

233 **3.2. Influence of sample preparation and the amount of sprayed matrix on the total ion**  
234 **current stabilization.** Avoiding the formation of hot spots due to inhomogeneous deposition of matrix  
235 is important to produce MS images of high quality. The KPMP Consortium (Veličković *et al.*), and  
236 Tressler *et al.* improved MALDI MSI data after factorial design optimization of the deposited matrix using  
237 an automatic sprayer on mice's kidney tissue sections<sup>24,37</sup>. In the presented work, the amount of  
238 deposited MALDI matrix was investigated in terms of signal suppression for the analytes of interest  
239 when varying the number of laser shots per pixel (see Figure S2). For this purpose, serial sagittal mouse  
240 brain slices were prepared with varying amounts of sprayed  $\alpha$ -HCCA matrix of 10 and 5 nmol per mm<sup>2</sup>  
241 respectively. MS images were acquired either using several hundreds of laser shots at 1000Hz (Figure  
242 1A) or using 6 laser shots at 60Hz (Figure 1B). In the latter, the laser focus of the solariX XR 9.4T  
243 Smartbeam II laser was adjusted from 98% to 80% to ablate and desorb an equivalent amount of

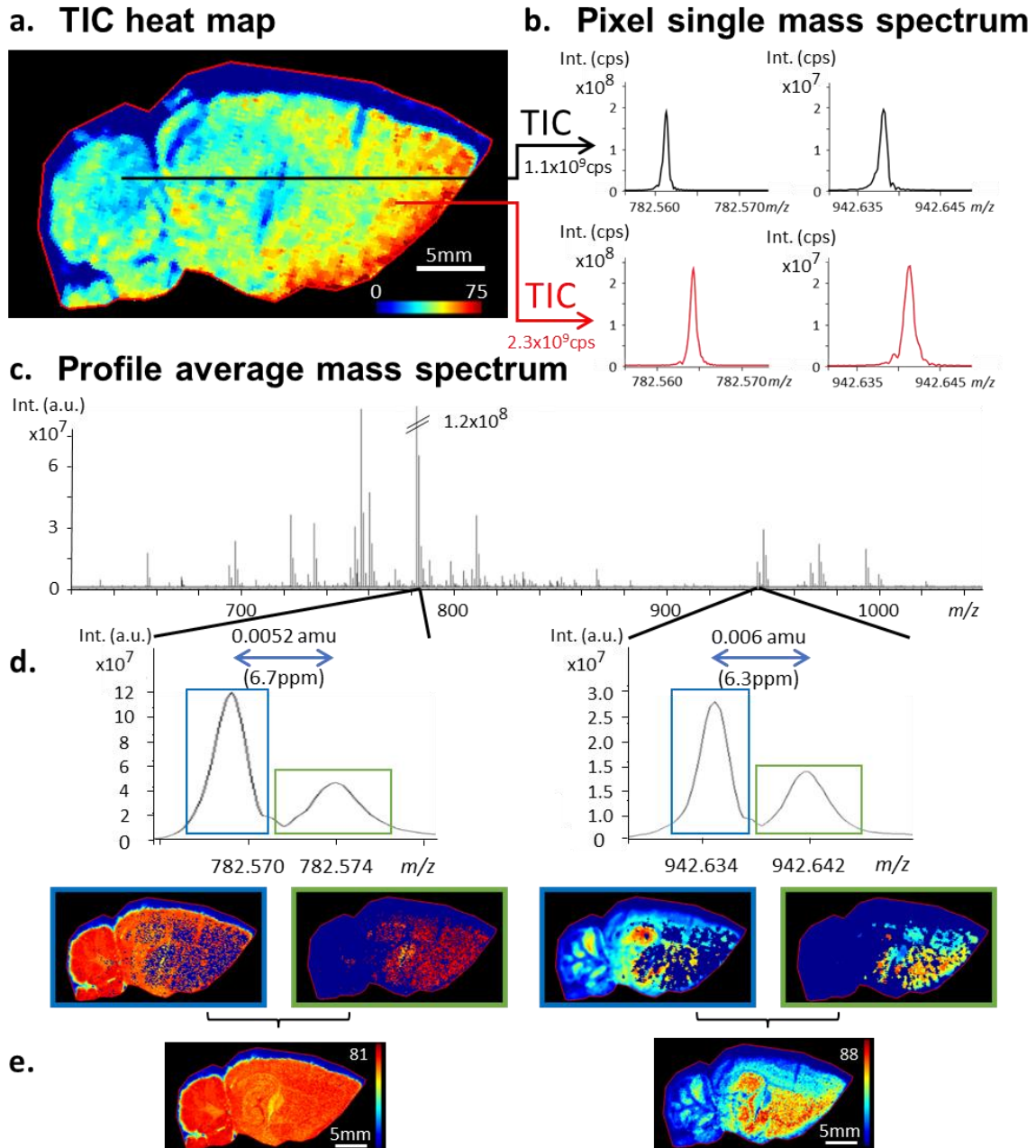
244 material per pixel. This allowed the generation of similar TIC values between the MALDI MSI methods.  
 245 Figure 1A shows an unstable TIC for the method employing sub-optimal parameters while the new set  
 246 of optimized settings showed a drastically improved TIC stability through the entire acquisition (Figure  
 247 1B). This resulted in improved alignment of the  $m/z$  peaks keeping the mass shifts below 0.5 ppm while  
 248 improving effective mass R.P. in the mean spectrum to around 400,000 at  $m/z$  400 for all detected ions  
 249 while keeping the same spatial resolution (Figure 1 A and B panel c). An in-house script has been used  
 250 to monitor the  $m/z$  channels for every pixel and compute the distribution of their measured values (apex  
 251 of the  $m/z$  peaks) and the R.P. using FWHM. Figure S3 provides a graphical representation of the mass  
 252 and R.P. distribution for  $m/z$  782.5674 ( $[PE\ 39:4+H]^+$  or  $[PC\ 36:4+H]^+$  (according to the LIPID MAPS  
 253 database) for both methods which were drastically improved when the TIC fluctuation was restrained.  
 254



255  
 256 **Figure 1. Comparison of dynamically harmonized MALDI FT-ICR MSI acquired on a solariX XR**  
 257 **9.4T with a manufacturer recommendation-based method (A) and a 6 laser shots-based method**  
 258 **(B), see section 3.2 for details. Reconstructed heat maps of the non-normalized Total Ion Count**  
 259 **of MS images (a). Portions of the TIC over time of the MSI acquisition and the computed mean**  
 260 **intensities with standard deviation (b). Observable gaps on the TIC are values from pixels**  
 261 **outside of the tissue section and were excluded to compute the standard deviation. The TIC**  
 262 **presented in the upper panel was obtained when 10nmol.mm<sup>-2</sup>  $\alpha$ -HCCA matrix was deposited**  
 263 **using 98% laser focus and from 5nmol.mm<sup>-2</sup>  $\alpha$ -HCCA matrix with 80% laser focus (lower panel).**  
 264 **Multi-pixel mass spectra overlay of  $m/z$  782.5674 shows the notable improvement in terms of**  
 265 **mass R.P. and mass accuracy measurements during the MALDI images between the unstable**  
 266 **(upper panel) and stable (lower panel) Total Ion Count (c).**

267 **3.3. ICR mass analyzer optimization and the influence of ion optic voltages on TIC stability.** At  
 268 first, the method employed was based on values recommended by the manufacturer for MALDI-MSI.  
 269 Minimal modifications were the use of the broadband mode in the 300 to 1200 amu mass range working  
 270 at an estimated R.P. above 400.000 at  $m/z$  800 with 4M data point. The solariX XR 9.4T instrument

271 was operated following a method optimized by Ferey *et al.*<sup>15</sup>. They optimized the MALDI FT-ICR MSI  
272 parameters using experimental designs from a 12T magnet instrument fitted with the Paracell. However,  
273 our MSI acquisitions performed on our 9.4T magnet suffered from severe mass shifts as shown in  
274 Figure 2. For individual pixels of the image, the experimental R.P. was slightly above the one estimated  
275 by the FT-ICR control software (FTMS control). Nevertheless, the centroids of the  $m/z$  peaks shifted  
276 from pixel-to-pixel resulting in an MMA below the specification of the instrument as observed in the  
277 profile average mass spectrum of the image. The MSI profile average spectrum showed peak  
278 broadening due to the combination of pixels mass spectra where a significant pixel-to-pixel mass shift  
279 of the measured  $m/z$  occurred. Extreme cases were observed where the  $m/z$  peaks were splitting by a  
280 few milli amus (i.e. several ppm) as shown in Figure 2d. The reconstructed MS images of  $m/z$  782.57  
281 (assumed to be [PC 34:1 + Na]<sup>+</sup>) and 942.64 (assumed to be [CL 36:4 + NH<sub>4</sub>]<sup>+</sup>), both selected with a  
282 mass tolerance of  $\pm 0.004$ , result in biased and incomplete ion distributions unless the targeted ions  
283 and their shifted counterparts  $m/z$  peak were selected together by extending the mass tolerance to  
284  $\pm 0.01$  for image reconstruction (Figure 2e). Comparison of the extracted spectra on a per-pixel basis  
285 (Figure 2a) showed that peak splitting could again be linked to the regions of interest submitted to large  
286 TIC variation despite the ion optics optimization adapted from Ferey *et al.* for our 9.4T instrument.



287

288 **Figure 2.** Heat map of the non-normalized TIC of a mouse brain section analyzed by high-  
 289 resolution MALDI FT-ICR MSI on a solarix XR 9.4T using non-optimized MSI method (a).  
 290 Extracted mass spectra from single pixels located in regions with significant differences in Total  
 291 Ion Current (b). Average mass spectrum (mean spectrum) of the whole MALDI image (c). Zoomed  
 292 profile average spectrum focused on  $m/z$  782.57 and 942.64 showing artifacts of split peaks and  
 293 their complementary distributions due to inconsistent mass measurement accuracy during  
 294 acquisition (d). Obtained localizations with a window selection encompassing both  $m/z$  peaks  
 295 shown in the vicinity of  $m/z$  782.57 and 942.64, respectively (e).

296 Ion optic voltages of the ICR mass analyzer were investigated as options to stabilize the TIC signal  
 297 (i.e. charge-space effects) in our 9.4T FT-ICR. Thus, investigations were focused on ICR parameters,  
 298 especially analyzer entrance, front and back trapping, sidekick, and excitation sweep voltages. Out of  
 299 those parameters, the sidekick was the only parameter that had a slight influence on the TIC stability.

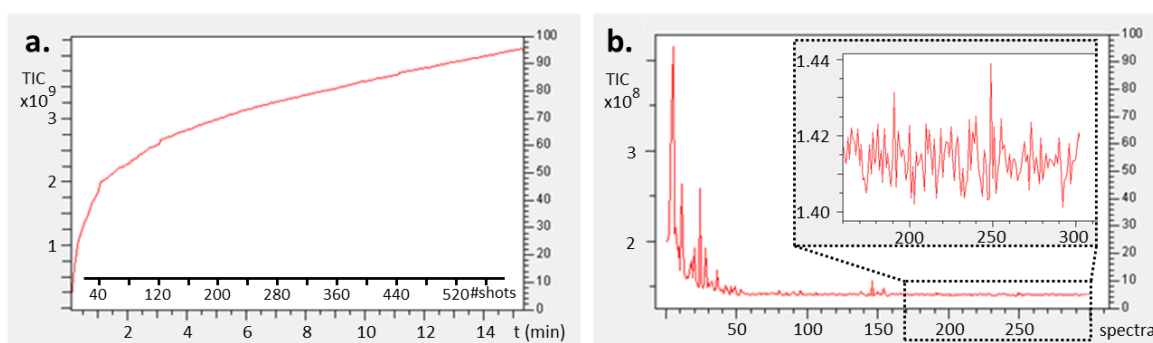
300 The sidekick offset optimization also showed a limited effect on the mass shift, while the front and back  
301 trapping, as well as the excitation sweep, affected the peak shapes (as expected) but not the TIC  
302 stability. In contrast, the voltage applied to the analyzer entrance had an effect. An increased analyzer  
303 entrance voltage was followed by a gradual decrease of the MS signal. We anticipate that it could  
304 potentially be used to limit the introduction of ions inside the ICR cell and act as a real-time ion injection  
305 control device. In the end, optimizing the ion optics does not significantly improve the TIC stability during  
306 MSI experiments.

307

308 **3.4. Monitoring MALDI processes and the influence of the number of laser shots.** Considering  
309 a scan being the event of acquiring a mass spectrum from the firing of one or more laser shots, the  
310 relationship between the TIC value and the number of laser shots per scan was investigated manually  
311 on mice brain tissue sections. Acquisitions ranging from the minimum number of laser shots per scan  
312 up to 600 laser shots on a fixed (x,y) position of the sample were performed. Because acquisitions with  
313 a single laser shot resulted in the absence of signals from both, the matrix and the tissue, 2 laser shots  
314 per scan were employed for the minimum number of laser shots per scan. Under this experimental  
315 condition, the laser frequency had to be lowered below 300Hz once again due to an absence of signal  
316 above this threshold. Below the laser frequency of 300Hz, no significant variations of the MS signal  
317 were observed (data not shown). To investigate the influence of the number of laser shots to produce  
318 adequate mass spectra for MSI, the laser shots to laser frequency ratio was kept at 1:10 resulting in a  
319 constant laser shots step duration. This 1:10 ratio ranges from 2 to 200 laser shots at a constant ratio  
320 because 2000 Hz is the operational limit of the SmartBeam II laser of the solariX XR and the scimaX  
321 2XR MALDI sources. By fixing the shooting duration, we should avoid most of the kinetic relaxation  
322 influences and balance the potential biases due to the ion extraction from the MALDI plume by the ion  
323 optics. Beyond 200 laser shots, the maximal laser frequency would be used at the cost of the constant  
324 shooting step duration.

325 Figure 3a shows the TIC accumulation (summed TIC) for 2 laser shots at 20Hz and Figure 3b shows  
326 the TIC value for each scan. Figure 3a indicates that most of the accumulated TIC signal (more than  
327 one-half) was obtained from the first 100 laser shots and that initial laser shots produced a rather linear  
328 increase in TIC, followed by a smaller amount of ions produced by subsequent laser shots. Then, a  
329 further linear increase is observed after about 120 laser shots due to the accumulation of mainly noise

330 peaks. Figure 3b points out a noticeable instability of the TIC during the 50 first laser shots. The very  
 331 first shots showed the highest signal abundance in the mass spectrum with a relatively high relative  
 332 abundance (> 10% relative intensity) which aligns with the so-called "first-shot phenomenon" first  
 333 described by the team of Hillenkamp<sup>38</sup>. The following laser shots, still ablating the same (x,y) position,  
 334 only poorly contributed to good signal-to-noise ratios for interesting  $m/z$  values and the less abundant  
 335  $m/z$  peaks vanished first. These results suggest that a smaller amount of laser shots is beneficial for  
 336 the detection of ions with an appropriate signal-to-noise ratio unless the targeted ions require a  
 337 significantly larger amount of laser energy to be detected. Thus, by using fewer laser shots TIC  
 338 fluctuations will be minimized to only a small percentage ensuring a more controlled number of ions to  
 339 be injected into the ICR cell. This leads to constant space-charge effects resulting in the production of  
 340 ultra-high mass R.P. MALDI images. The contribution of the laser shots and the desorption/ionization  
 341 steps of each pixel being imaged in terms of duration is typically less than 1 second from 2 to 10 laser  
 342 shots when operating the laser shots to laser frequency at a 1:10 constant ratio.



343

344 **Figure 3. Accumulated Total Ion Current over time (a) and Total Ion Current per scan (b) for a**  
 345 **300 scans acquisition with a setting of 2 laser shots at 20Hz per scan performed on a**  
 346 **dynamically harmonized MALDI FT ICR solarix XR 9.4T.**

347 **3.5. Influence of the number of laser shots for the apparent dynamic range of imaged lipids.** New  
 348 sets of mice brain images were produced by MALDI MSI. The number ranged from 10 to 600 at a fixed  
 349 laser-shooting time duration (i.e. laser shots to laser frequency ratio). As expected, lowering the number  
 350 of laser shots (from 600 to 10) reduced the overall signal intensities in the mass spectra (TIC) although  
 351 the detected ions for both methods were comparable. The loss of  $m/z$  signals in the method using the  
 352 lower amount of laser shots was mainly concerning the isotope contributions and peaks that were  
 353 already close to the  $3 \times S/N$  (signal over noise) as computed by the software. Interestingly, the absolute  
 354 intensities of the minor ions were almost not affected compared to the most abundant ones when using  
 355 fewer laser shots and  $5 \text{ nmol} \cdot \text{mm}^{-2}$  of deposited matrix on mice's brain tissue sections. Table 2 reports  
 356 the absolute intensity, mass accuracy, and intensity ratio between high and low abundant lipids  
 357 detected in the MS images of mice's brain tissue section when using 10 or 100 laser shots. The lipids  
 358 were identified according to LIPID MAPS database peak annotation. Ions at  $m/z$  772.53 and 798.54

359 were the most intense signals observed while  $m/z$  770.51 and 848.56 are among the least intense ions.  
 360 When comparing 10 to 100 laser shots, the intensities of minor ions were roughly halved while major  
 361 ions intensities decrease by an order of magnitude. By reducing the number of laser shots per scan the  
 362 relative intensities of the most intense ions tend to decrease to a larger extent in regards to the less  
 363 intense ions. Any combination of intense/less intense ion ratios leads to the same observations.  
 364 Besides, the intensity ratio between ions of comparable intensities (e.g.  $m/z$  772.53 vs 798.54) was  
 365 almost unaffected by the number of laser shots per scan.

366 **Table 2. Intensities and ratios of detected and identified lipids in a mouse brain tissue section**  
 367 **acquired with the MALDI FT-ICR MS (solariX XR 9.4T) instrument for 10 and 100 laser shots**

Target m/z	Identification	10 shots				100 shots			
		Intensity (c.p.s)	Mass accuracy (ppm)	Ratio m/z 772.53 over m/z target	Ratio m/z 798.54 over m/z target	Intensity (c.p.s)	Mass accuracy (ppm)	Ratio m/z 772.53 over m/z target	Ratio m/z 798.54 over m/z target
770.50975	[PA 36:2+K] <sup>+</sup>	4.8E+05	-0.09	10.6	11.3	1.3E+06	-0.12	33.1	40.0
848.55643	[PC 38:4+K] <sup>+</sup>	8.9E+05	-0.25	5.73	6.07	6.5E+06	-0.24	6.61	8.00
772.52519	[PC 32:0+K] <sup>+</sup>	5.1E+06	-0.13		1.06	4.3E+07	-0.17		1.21
798.54079	[PC 34:1+K] <sup>+</sup>	5.4E+06	-0.26	0.94		5.2E+07	-0.26	0.83	

368  
 369 The cause of the disparity in the ion intensity ratio when varying the number of laser shots was  
 370 further investigated. It could indeed be related to either, the ionization process itself or the efficiency of  
 371 ion transmission by the ion optics and/or the MS analyzer (ICR cell). Similar experiments to determine  
 372 the influence of the ionization process were conducted on a MALDI-ToF instrument (rapifleX, Bruker,  
 373 Germany) despite its differences in terms of ion extraction mechanism, source vacuum, and laser  
 374 compared to the solariX XR and the scmiaX 2XR. To be somehow comparable with the Smartbeam II,  
 375 the beamscan option of the Smartbeam 3D was not used which avoids the laser energy being swept at  
 376 the surface of the sample (i.e. matrix blaster). No variation of the ion intensity ratio was observed with  
 377 the MALDI-ToF as shown in Table 3, despite we used a maximum of 1000 laser shots accumulation  
 378 instead of 100, regardless of the major or minor ions considered. The ablated surface of the sample of  
 379 only 25 $\mu$ m<sup>2</sup> with only 10 laser shots allowed the less abundant ions to still be detected and only matrix  
 380 signal intensities were strongly affected. The variation of the ion ratio observed with the MALDI FT-ICR  
 381 was then related to the ion optics and/or the ICR mass analyzer. It is worth reminding that higher  
 382 magnetic fields improve the dynamic range of the number of trapped ions inside the ICR in the absence  
 383 of noticeable space charge effects.

384 **Table 3. Intensities and ratio of detected and identified lipids in a mouse brain tissue section**  
 385 **acquired with the MALDI ToF MS (rapifleX) instrument (external calibration, enhanced cubic**  
 386 **regression) for 10 and 1000 laser shots with the single focus option and without beamscan**

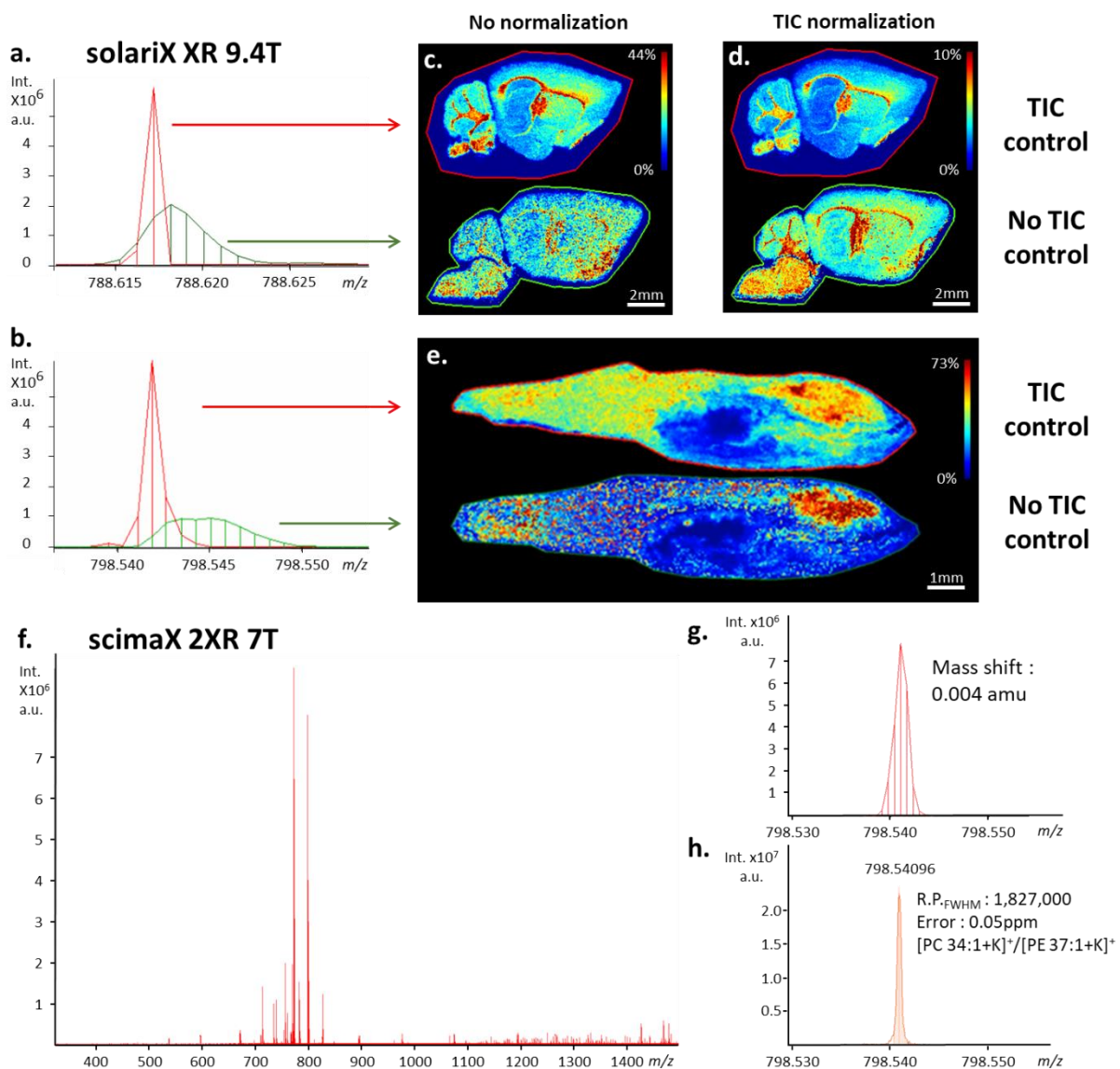
Target m/z	Identification	10 shots				1000 shots			
		Intensity (c.p.s)	Mass accuracy (ppm)	Ratio m/z 782.57 over m/z target	Ratio m/z 798.54 over m/z target	Intensity (c.p.s)	Mass accuracy (ppm)	Ratio m/z 782.57 over m/z target	Ratio m/z 798.54 over m/z target
782.567	[PC 36:4+H] <sup>+</sup>	6.8E+03	+9.7		0.79	1.8E+04	+7.1		0.81
798.541	[PC 34:1+K] <sup>+</sup>	5.3E+03	+11.2	1.27		1.5E+04	+10.0	1.23	
806.567	[PS 37:0+K] <sup>+</sup>	4.0E+03	-12.3	1.68	1.33	9.7E+03	-11.1	1.90	1.54
844.546	[PC 36:3+Na] <sup>+</sup>	4.6E+03	+3.8	1.47	1.16	1.5E+04	6.2	1.22	0.99

387  
388

389 **3.6. Robustness of the MALDI MSI at ultra-high mass R.P. using the MALDI FT-ICR solariX XR**

390 **9.4T.** When applying the optimized method for extreme resolution MSI with an estimated R.P. over  
 391 500,000 at  $m/z$  800 (>1,000,000 at  $m/z$  400), a much less pronounced mass shift was observed and  
 392 most importantly is fully within the instrument specifications ( $\pm 0.5$ ppm) even for profile and centroided  
 393 average MALDI image spectra. FWHM resolutions for the individual spectra are now similar to the ones  
 394 observed in the profile average spectrum. The acquisition of such mass spectra qualities during an MSI  
 395 experiment of rat brain samples was previously achieved using a custom prototype of a hybrid linear  
 396 ion trap coupled to a 21T supra conducting magnet fitted with the Paracell by the NHMFL group at  
 397 Tallahassee in Florida<sup>39</sup>. In this work, comparable results were obtained in terms of MSI mass R.P. and  
 398 MMA with a superconducting magnet of 9.4T using the same ICR cell (see Table S1). By comparing  
 399 the average spectrum of centroided MSI data performed on serial brain (Figure 4a) and whole-body  
 400 zebrafish sections (Figure 4b), the difference in image quality is clearly evident. The new method with  
 401 a controlled ion injection in the cell (TIC stabilized) resulted in narrow  $m/z$  peaks due to a significantly  
 402 reduced mass shift. The image of the ion distribution in the tissue section is also less noisy whether or  
 403 not TIC or RMS normalized (RMS not shown). To demonstrate the robustness of the controlled TIC  
 404 method, replicates of serial brain sections (roughly 12,000 pixels) and zebrafish whole body sections  
 405 (roughly 20,000 pixels) were acquired using our optimized method (see Figure S5). In all cases, the  
 406 experimental mass R.P. expected by the acquisition software was surpassed. The imaging method was  
 407 tested for images with  $R.P.FWHM$  beyond 1,000,000 at  $m/z$  800 for the brain region of the zebrafish  
 408 sample (roughly 1500 pixels). Figure S6 shows observable isotopic fine structures for abundant ions

409 also observable in the profile average spectrum further increasing the confidence of the identification  
 410 process of these ions. Note that a slight loss in R.P. is still observed in the profile average spectrum  
 411 compared to individual pixels spectra even with a contained mass shift below 0.5ppm (i.e. in agreement  
 412 with the instrument specification). At such high R.P. the contribution of a mass shift of 0.5ppm at  $m/z$   
 413 800 (i.e. 0.4 amu) is still impacting negatively the R.P. In complement, a peak realignment strategy  
 414 by software post-processing coupled with our proposed MSI method was developed in our group to  
 415 restore the isotopic fine structure also in the average mass spectrum of MS images having lower mass  
 416 R.P.<sup>40,41</sup>.



417  
 418 **Figure 4. Centroided average MSI mass spectra of mouse brain (a) and zebrafish (b) using a**  
 419 **MALDI FT-ICR (solarix XR 9.4T, fitted with ParaCell) instrument, zoomed in on  $m/z$  788,62 and**  
 420 **798.54 respectively, showing peak width differences due to MMA obtained with (red) and without**  
 421 **(green) TIC stabilization by optimization of the laser shot number (6 laser shots at 60 Hz).**

422 **Reconstructed MS images without (c) and with (d) TIC normalization, applying or not applying**  
423 **TIC stabilization. Centroided average MSI mass spectrum of a mouse brain tissue section**  
424 **acquired on the scimaX 2XR using the  $2\omega$  detection mode with TIC stabilization (f). Zoom in to**  
425  **$m/z$  798.54 showing peak width difference due to MMA (h). Zoom on  $m/z$  798.54 in an extracted**  
426 **pixel spectrum showing the obtained R.P. FWHM and MMA. See text for details.**

427

428 **3.7. Influence of the magnetic field strength.** FT-ICR operating at a high magnetic field ( $\geq 12$ T) are  
429 typically used for petroleomics analysis by direct infusion electrospray ionization analysis of diluted raw  
430 crude oils. Direct infusion allows for a stable TIC signal and fills the ICR cell with a constant number of  
431 ions at each scan. Higher magnetic fields allow the storage of a larger number of ions but also a stable  
432 ion motion during long transient signal acquisition enabling very high mass R.P. ( $\geq 1,000,000$  at  $m/z$   
433 400). Recently Ge *et al*<sup>42</sup> demonstrated for oil samples introduced by direct infusion the capability of  
434 FT-ICR mass analyzers operating at 7T and  $2\omega$  detection to closely match the performance of a 15T  
435 instrument. MSI also takes advantage of greater magnetic fields to produce higher quality images<sup>15,39</sup>.  
436 In this work, the influence of TIC variation was investigated for an FT-ICR instrument equipped with a  
437 ParaCell but using lower magnetic field strength, i.e. 7T. The scimaX 2XR 7T instrument also provides  
438 the  $2\omega$  detection mode which recycles the excitation plates into detection plates to improve the duty  
439 cycle (transient signal) by a factor of 2 compared to the  $1\omega$  detection mode. Mice brain images were  
440 compared for both  $1\omega$  and  $2\omega$  detection. Also, for this instrument, TIC control improved the MMA and  
441 spectral resolutions (See Figure 4f, g, h, and Figure S7). Interestingly, while no direct influence on ion  
442 current stability was observed when the  $2\omega$  detection mode was activated (Figure S8a), the mass shift  
443 was easier to constrain compared to  $1\omega$  mode datasets (Figure S8b). We assumed that the drastic  
444 diminution of the transient signal duration prevented peak coalescence as well as the decoherence of  
445 the ion packets inside the ICR cell<sup>8,43</sup>. It is worth mentioning that the comparison of MS images  
446 performed on serial tissue sections using  $1\omega$  and  $2\omega$  detection mode showed no tangible differences  
447 in terms of co-localization of the observed ions (Figure S8b). As an illustration, an MS image acquired  
448 with the solariX 9.4T and the scimaX 2XR 7T using the  $2\omega$  detection mode at 16M data points of 1000  
449 pixels of mouse brain tissue section showed an R.P.<sub>FWHM</sub> above 1,500,000 at  $m/z$  800 and an MMA of  
450 0.15ppm (Figure 4 f, g, and h). The typical time to produce an image of 1000 pixels was 195 minutes  
451 using our solariX XR 9.4T (i.e.  $1\omega$  at 8M data point) and 205 minutes using the scimaX 2XR 7T operating  
452 at  $2\omega$  and 16M data point.

453 Table 4 shows the dynamic range obtained for high and low abundant lipid signals detected during  
 454 the MSI experiment of 2 consecutive brain sections with the scimaX 2XR using 1 or 2 $\omega$  detection mode.  
 455 Note that the 7T instrument still required the ICR cell to be loaded with fewer ions than the 9.4T  
 456 instrument using 1 $\omega$  or 2 $\omega$  detection to restrict the experimental mass shift in average mass spectra.  
 457 Therefore, fewer laser shots were used to produce the data in Table 4 compared to Table 2 and Table  
 458 3. The ratios obtained for the scimaX 2XR using 1 $\omega$  detection are somewhat similar to what was  
 459 obtained with the 9.4T solariX XR. The 2 $\omega$  detection mode seems to be also beneficial because the  
 460 dynamic range of the lipids detected in the MALDI images was less affected than the 1 $\omega$  detection  
 461 mode. The higher power of the magnet is still beneficial for reaching a wider intra-scan dynamic range,  
 462 or if the TIC cannot be efficiently stabilized, even after optimizing the laser parameters. Nevertheless,  
 463 MSI acquisition at extreme mass R.P. is possible using the 7T superconducting magnet and 2 $\omega$   
 464 detection.

465

466 **Table 4. Intensities and ratio of detected and identified lipids in a mouse brain tissue section**  
 467 **acquired with the MALDI FT-ICR-MS (scimaX 2XR 7T) instrument for 6 and 400 laser shots**

Target m/z	Identification	6 laser shots				400 laser shots			
		Intensity (c.p.s)	Mass Accuracy (ppm)	Ratio m/z (a) over m/z target	Ratio m/z (b) over m/z target	Intensity (c.p.s)	Mass Accuracy (ppm)	Ratio m/z (a) over m/z target	Ratio m/z (b) over m/z target
<b>scimaX 2XR 7T, 1<math>\omega</math> detection mode</b>									
713.45181	[PA 34:1+K] <sup>+</sup>	8.0E+5	+0.40	6.63	30.0	2.7E+6	+0.61	7.04	18.5
844.52531	[PC 38:6+K] <sup>+</sup>	2.4E+5	+0.53	22.1	100	Not detected	+0.58	N.C.	N.C.
772.52519	[PC 32:0+K] <sup>+</sup>	5.3E+6	+0,37		4.53	1.9E+7	+0.56		2.63
798.54079	[PC 34:1+K] <sup>+</sup>	2.4E+7	+0.26	0.22		5.0E+7	+0.44	0.38	
<b>scimaX 2XR 7T, 2<math>\omega</math> detection mode</b>									
713.45181	[PA 34:1+K] <sup>+</sup>	4.3E+6	+0.23	3.72	4.88	4.9E+6	+0.40	4.29	10.4
844.52531	[PC 38:6+K] <sup>+</sup>	3.9E+6	+0.17	4.10	5.38	4.3E+6	+0.33	3.13	7.61
772.52519	[PC 32:0+K] <sup>+</sup>	1.6E+7	+0,22		1.31	2.1E+7	+0.37		2.43
798.54079	[PC 34:1+K] <sup>+</sup>	2.1E+7	+0.26	0.76		6.7E+7	+0.31	0.41	

468 *m/z* (a) corresponds to 772,53 and *m/z* (b) correspond to 798,54

469 N.C. Not Computed

470 **3.8. Improvement of peak annotation.** Lastly, database queries for mass lists obtained with the  
 471 optimized method showed an improvement in terms of peak annotations: fewer false positives and  
 472 negatives were observed due to the improved R.P., and MMA. Figure S9 shows some examples of

473 database results as histograms of the matching counts at a given mass accuracy (in ppm) to detect  
474 readily any oddities in the dataset. When the TIC was not stabilized (not optimized method), most of  
475 the identifications had mass accuracy around -1.5 ppm. These values were not consistent with the  
476 specification of a properly calibrated FT-ICR instrument and they do not fit with the requirement for  
477 proper annotation of lipids from the LIPID MAPS database. In contrast, the MALDI image acquired with  
478 the optimized method and stabilized TIC led to a larger number of identifications, with scores around  
479 +0.4ppm that are well within the nominal performance for the instrument. The number of total matches  
480 is drastically improved due to fewer false-negative identifications and similarly, potentially fewer false-  
481 positive results. Of course, the addition of the isotopic fine structure further improved the confidence  
482 level of the identified lipids.

#### 483 **4. Conclusion**

484 In this work, we successfully limited the space-charge effects and limited the resulting mass shift to  
485 improve mass accuracy for MALDI MS images of mouse brains and Zebrafish tissue sections by  
486 introducing a controlled TIC injection method in the ICR cell. The method was successfully applied on  
487 the solariX XR 9.4T and the scimaX 2XR 7T, two commercially available dual-source ESI/MALDI  
488 instruments fitted with the Paracell®. Under optimal instrumental settings, this was achieved primarily  
489 by optimizing lasers parameters and the concentration of deposited/sprayed matrix. MSI with a  
490 resolving mass power beyond 1,000,000 at  $m/z$  800 was successfully achieved within around 200  
491 minutes for 1000 imaged pixels (transient duration of 11.7sec at 8M data points in an operated mass  
492 range between  $m/z$  300 and 1200 using the common Amplitude mode for the solariX XR 9.4T, and a  
493 transient of 12.3sec for the scimaX 2XR 7T in 2 $\omega$  detection mode at 16M data points) with no mass  
494 shift beyond 1 ppm (typical mass shift < 0.5ppm) which correlates to approximately 0.5 mamu in the  
495 lipid mass range. The resulting images were less noisy, i.e. showing higher contrast and appearing by  
496 this to be sharper, at constant lateral resolution and matrix deposition method. Extreme resolution MS  
497 images obtained with relatively limited power of magnetic fields (< 12T) require a stabilized TIC  
498 throughout the acquisition to retain the instrument specifications. The intra-scan dynamic range  
499 obtained during this work using the commercially available 9.4T and 7T instruments seemed to be  
500 around 100, while Bowman *et al.*<sup>39</sup> reported a dynamic range of around 500 using a custom 21T MALDI  
501 FT-ICR instrument. Using 2 $\omega$  detection on higher magnetic field instruments will speed up the scan

502 time by a factor of 2, allowing more samples to be measured at constant mass R.P. in the same time  
503 frame. Peak annotations using the LIPID MAPS database correspond to identification scores better  
504 than 0.4ppm, limiting misidentification of lipids, especially for measurement generating isotopic fine  
505 structures. Revisiting the laser parameters improved method reproducibility from pixels-to-pixels and  
506 also from sample-to-sample, which improved the robustness of our method by successfully performing  
507 similar MALDI images of consecutive tissue sections in replicates.

508 It was found that the entrance voltage to the analyzer affects the number of ions introduced into the  
509 ICR cell in an interesting way that could potentially be used to limit the overflow of ions to be injected  
510 into the ICR cell, acting as an ion injection control device. The idea would be to limit ion current  
511 fluctuations in real-time for samples with high concentration heterogeneity of target compounds. This  
512 would require further investigation as it is currently considered a double-edged sword, as the signal can  
513 be easily lost if this voltage value is not properly set.

#### 514 **Acknowledgments**

515 This work was supported by the Eurlipids Interreg V-A Euregio Meuse-Rhine with support from the  
516 European Fund for Regional Development of the European Union ([www.eurlipids.com](http://www.eurlipids.com)). This work was  
517 also a contribution to the EU Horizon 2020 research and Innovation program under grant agreement  
518 N° 731077 and the European Project EU\_FT-ICR\_MS (H2020 INFRAIA-02-2017). The MALDI ToF  
519 rapifleX and the MALDI FT-ICR solariX XR were co-funded by FEDER BIOMED HUB Technology  
520 Support (number 2.2.1/996). This work was also a contribution to ZonMw Memorabel program (number:  
521 733050105), Cost action under grant CA16122 – BIONECA and Hersenstichting (number: DR-2018-  
522 00274). The scimaX 7T 2XR was funded by TU Wien and the Federal Ministry Republic of Austria for  
523 Education, Science and Research (HRSM2016). This work was also a contribution to the Christian  
524 Doppler Laboratory for Skin Multimodal Imaging of Aging and Senescence (SkinMAGINE) and the  
525 Austrian Science Foundation project ChemTalk (P32179-B). All experiments were performed with  
526 permission from the Committee on Animal Welfare of Maastricht University and the Committee on  
527 Animal Welfare of Liege University, according to Dutch or Belgian governmental legislation,  
528 respectively.

529

530

531 **References**

- 532 (1) Le Rhun, E.; Duhamel, M.; Wisztorski, M.; Gimeno, J.-P.; Zairi, F.; Escande, F.; Reyns, N.;  
533 Kobeissy, F.; Maurage, C.-A.; Salzet, M.; Fournier, I. Evaluation of Non-Supervised MALDI  
534 Mass Spectrometry Imaging Combined with Microproteomics for Glioma Grade III  
535 Classification. *Biochimica et Biophysica Acta (BBA) - Proteins and Proteomics* **2017**, *1865* (7),  
536 875–890.
- 537 (2) Ellis, S. R.; Cappell, J.; Potočnik, N. O.; Balluff, B.; Hamaide, J.; Van der Linden, A.; Heeren,  
538 R. M. A. More from Less: High-Throughput Dual Polarity Lipid Imaging of Biological Tissues.  
539 *Analyst* **2016**, *141* (12), 3832–3841.
- 540 (3) Lamont, L.; Eijkel, G. B.; Jones, E. A.; Flinders, B.; Ellis, S. R.; Porta Siegel, T.; Heeren, R. M.  
541 A.; Vreeken, R. J. Targeted Drug and Metabolite Imaging: Desorption Electrospray Ionization  
542 Combined with Triple Quadrupole Mass Spectrometry. *Anal. Chem.* **2018**, *90* (22), 13229–  
543 13235.
- 544 (4) Wang, J.; Wang, C.; Han, X. Tutorial on Lipidomics. *Analytica Chimica Acta* **2019**, *1061*, 28–  
545 41. <https://doi.org/10.1016/j.aca.2019.01.043>.
- 546 (5) Marshall, A. G.; Hendrickson, C. L. High-Resolution Mass Spectrometers. *Annual Rev. Anal.*  
547 *Chem.* **2008**, *1* (1), 579–599.
- 548 (6) Kostyukevich, Y. I.; Vladimirov, G. N.; Nikolaev, E. N. Dynamically Harmonized FT-ICR Cell  
549 with Specially Shaped Electrodes for Compensation of Inhomogeneity of the Magnetic Field.  
550 Computer Simulations of the Electric Field and Ion Motion Dynamics. *J. Am. Soc. Mass*  
551 *Spectrom.* **2012**, *23* (12), 2198–2207.
- 552 (7) Nikolaev, E. N.; Kostyukevich, Y. I.; Vladimirov, G. N. Fourier Transform Ion Cyclotron  
553 Resonance (FT ICR) Mass Spectrometry: Theory and Simulations: FT ICR MS. *Mass Spec Rev*  
554 **2016**, *35* (2), 219–258.
- 555 (8) Boldin, I. A.; Nikolaev, E. N. Fourier Transform Ion Cyclotron Resonance Cell with Dynamic  
556 Harmonization of the Electric Field in the Whole Volume by Shaping of the Excitation and  
557 Detection Electrode Assembly: New Principle of Ion Detection in a FTICR Penning Trap. *Rapid*  
558 *Commun. Mass Spectrom.* **2011**, *25* (1), 122–126.
- 559 (9) Jertz, R.; Friedrich, J.; Kriete, C.; Nikolaev, E. N.; Baykut, G. Tracking the Magnetron Motion in  
560 FT-ICR Mass Spectrometry. *J. Am. Soc. Mass Spectrom.* **2015**, *26* (8), 1349–1366.
- 561 (10) Popov, I. A.; Nagornov, K.; N.Vladimirov, G.; Kostyukevich, Y. I.; Nikolaev, E. N. Twelve Million  
562 Resolving Power on 4.7 T Fourier Transform Ion Cyclotron Resonance Instrument with  
563 Dynamically Harmonized Cell—Observation of Fine Structure in Peptide Mass Spectra. *J. Am.*  
564 *Soc. Mass Spectrom.* **2014**, *25* (5), 790–799.
- 565 (11) Nikolaev, E. N.; Gorshkov, M. V.; Mordehai, A. V.; Talrose, V. L. Ion Cyclotron Resonance  
566 Signal-Detection at Multiples of the Cyclotron Frequency. *Rapid Commun. Mass Spectrom.*  
567 **1990**, *4* (5), 144–146.
- 568 (12) Pan, Y.; Ridge, D. P.; Rockwood, A. L. Harmonic Signal Enhancement in Ion Cyclotron  
569 Resonance Mass Spectrometry Using Multiple Electrode Detection. *International Journal of*  
570 *Mass Spectrometry and Ion Processes* **1988**, *84* (3), 293–304.
- 571 (13) Schweikhard, L. Theory of Quadrupole Detection Fourier Transform-Ion Cyclotron Resonance.  
572 *International Journal of Mass Spectrometry and Ion Processes* **1991**, *107* (2), 281–292.
- 573 (14) Pan, Y.; Ridge, D. P.; Wronka, J.; Rockwood, A. L.; Marshall, A. G. Resolution Improvement by  
574 Using Harmonic Detection in an Ion Cyclotron Resonance Mass Spectrometer. *Rapid Commun.*  
575 *Mass Spectrom.* **1987**, *1* (7–8), 120–121.
- 576 (15) Ferey, J.; Marguet, F.; Laquerrière, A.; Marret, S.; Schmitz-Afonso, I.; Bekri, S.; Afonso, C.;  
577 Tebani, A. A New Optimization Strategy for MALDI FTICR MS Tissue Analysis for Untargeted  
578 Metabolomics Using Experimental Design and Data Modeling. *Anal Bioanal Chem* **2019**, *411*  
579 (17), 3891–3903.
- 580 (16) Longuespée, R.; Kriegsmann, K.; Cremer, M.; Zgorzelski, C.; Casadonte, R.; Kazdal, D.;  
581 Kriegsmann, J.; Weichert, W.; Schwamborn, K.; Fresnais, M.; Schirmacher, P.; Kriegsmann,  
582 M. In MALDI-Mass Spectrometry Imaging on Formalin-Fixed Paraffin-Embedded Tissue

- 583 Specimen Section Thickness Significantly Influences *m/z* Peak Intensity. *Prot. Clin. Appl.* **2019**,  
584 13 (1), 1800074.
- 585 (17) Goodwin, R. J. A. Sample Preparation for Mass Spectrometry Imaging: Small Mistakes Can  
586 Lead to Big Consequences. *Journal of Proteomics* **2012**, 75 (16), 4893–4911.
- 587 (18) Shimma, S.; Sugiura, Y. Effective Sample Preparations in Imaging Mass Spectrometry. *Mass*  
588 *Spectrometry* **2014**, 3 (Special\_Issue), S0029–S0029.
- 589 (19) Morikawa-Ichinose, T.; Fujimura, Y.; Murayama, F.; Yamazaki, Y.; Yamamoto, T.; Wariishi, H.;  
590 Miura, D. Improvement of Sensitivity and Reproducibility for Imaging of Endogenous  
591 Metabolites by Matrix-Assisted Laser Desorption/Ionization-Mass Spectrometry. *J. Am. Soc.*  
592 *Mass Spectrom.* **2019**, 30 (8), 1512–1520.
- 593 (20) Kaletaş, B. K.; van der Wiel, I. M.; Stauber, J.; Lennard J. Dekker; Güzel, C.; Kros, J. M.; Luider,  
594 T. M.; Heeren, R. M. A. Sample Preparation Issues for Tissue Imaging by Imaging MS: Sample  
595 Preparation Issues for Tissue Imaging. *Proteomics* **2009**, 9 (10), 2622–2633.
- 596 (21) Grassl, J.; Taylor, N. L.; Millar, Ah. Matrix-Assisted Laser Desorption/Ionisation Mass  
597 Spectrometry Imaging and Its Development for Plant Protein Imaging. *Plant Methods* **2011**, 7  
598 (1), 21.
- 599 (22) Nishidate, M.; Hayashi, M.; Aikawa, H.; Tanaka, K.; Nakada, N.; Miura, S.; Ryu, S.; Higashi, T.;  
600 Ikarashi, Y.; Fujiwara, Y.; Hamada, A. Applications of MALDI Mass Spectrometry Imaging for  
601 Pharmacokinetic Studies during Drug Development. *Drug Metabolism and Pharmacokinetics*  
602 **2019**, 34 (4), 209–216.
- 603 (23) Prideaux, B.; Stoeckli, M. Mass Spectrometry Imaging for Drug Distribution Studies. *Journal of*  
604 *Proteomics* **2012**, 75 (16), 4999–5013.
- 605 (24) Tressler, C.; Tilley, S.; Yang, E.; Donohue, C.; Barton, E.; Creissen, A.; Glunde, K. Factorial  
606 Design to Optimize Matrix Spraying Parameters for MALDI Mass Spectrometry Imaging. *J. Am.*  
607 *Soc. Mass Spectrom.* **2021**, 32 (12), 2728–2737.
- 608 (25) Römpf, A.; Guenther, S.; Schober, Y.; Schulz, O.; Takats, Z.; Kummer, W.; Spengler, B.  
609 Histology by Mass Spectrometry: Label-Free Tissue Characterization Obtained from High-  
610 Accuracy Bioanalytical Imaging. *Angewandte Chemie International Edition* **2010**, 49 (22),  
611 3834–3838.
- 612 (26) Barry, J. A.; Robichaud, G.; Muddiman, D. C. Mass Recalibration of FT-ICR Mass Spectrometry  
613 Imaging Data Using the Average Frequency Shift of Ambient Ions. *J. Am. Soc. Mass Spectrom.*  
614 **2013**, 24 (7), 1137–1145.
- 615 (27) Smith, D. F.; Kharchenko, A.; Konijnenburg, M.; Klinkert, I.; Paša-Tolić, L.; Heeren, R. M. A.  
616 Advanced Mass Calibration and Visualization for FT-ICR Mass Spectrometry Imaging. *J. Am.*  
617 *Soc. Mass Spectrom.* **2012**, 23 (11), 1865–1872.
- 618 (28) Youmans, K. L.; Tai, L. M.; Nwabuisi-Heath, E.; Jungbauer, L.; Kanekiyo, T.; Gan, M.; Kim, J.;  
619 Eimer, W. A.; Estus, S.; Rebeck, G. W.; Weeber, E. J.; Bu, G.; Yu, C.; LaDu, M. J. APOE4-  
620 Specific Changes in A $\beta$  Accumulation in a New Transgenic Mouse Model of Alzheimer Disease.  
621 *Journal of Biological Chemistry* **2012**, 287 (50), 41774–41786.
- 622 (29) Oakley, H.; Cole, S. L.; Logan, S.; Maus, E.; Shao, P.; Craft, J.; Guillozet-Bongaarts, A.; Ohno,  
623 M.; Disterhoft, J.; Van Eldik, L.; Berry, R.; Vassar, R. Intraneuronal Beta-Amyloid Aggregates,  
624 Neurodegeneration, and Neuron Loss in Transgenic Mice with Five Familial Alzheimer's  
625 Disease Mutations: Potential Factors in Amyloid Plaque Formation. *Journal of Neuroscience*  
626 **2006**, 26 (40), 10129–10140.
- 627 (30) Goodwin, R. J. A.; Pennington, S. R.; Pitt, A. R. Protein and Peptides in Pictures: Imaging with  
628 MALDI Mass Spectrometry. *Proteomics* **2008**, 8 (18), 3785–3800.
- 629 (31) Sládková, K.; Houška, J.; Havel, J. Laser Desorption Ionization of Red Phosphorus Clusters  
630 and Their Use for Mass Calibration in Time-of-Flight Mass Spectrometry. *Rapid Commun. Mass*  
631 *Spectrom.* **2009**, 23 (19), 3114–3118.
- 632 (32) Fahy, E.; Sud, M.; Cotter, D.; Subramaniam, S. LIPID MAPS Online Tools for Lipid Research.  
633 *Nucleic Acids Research* **2007**, 35 (Web Server), W606–W612.
- 634 (33) Sud, M.; Fahy, E.; Cotter, D.; Brown, A.; Dennis, E. A.; Glass, C. K.; Merrill, A. H.; Murphy, R.

635 C.; Raetz, C. R. H.; Russell, D. W.; Subramaniam, S. LMSD: LIPID MAPS Structure Database.  
636 *Nucleic Acids Research* **2007**, *35* (Database), D527–D532.

637 (34) Fahy, E.; Subramaniam, S.; Brown, H. A.; Glass, C. K.; Merrill, A. H.; Murphy, R. C.; Raetz, C.  
638 R. H.; Russell, D. W.; Seyama, Y.; Shaw, W.; Shimizu, T.; Spener, F.; van Meer, G.;  
639 VanNieuwenhze, M. S.; White, S. H.; Witztum, J. L.; Dennis, E. A. A Comprehensive  
640 Classification System for Lipids. *Journal of Lipid Research* **2005**, *46* (5), 839–861.

641 (35) Francl, T. J.; Sherman, M. G.; Hunter, R. L.; Locke, M. J.; Bowers, W. D.; McIver, R. T.  
642 Experimental Determination of the Effects of Space Charge on Ion Cyclotron Resonance  
643 Frequencies. *International Journal of Mass Spectrometry and Ion Processes* **1983**, *54* (1–2),  
644 189–199.

645 (36) Easterling, M. L.; Mize, T. H.; Amster, I. J. Routine Part-per-Million Mass Accuracy for High-  
646 Mass Ions: Space-Charge Effects in MALDI FT-ICR. *Anal. Chem.* **1999**, *71* (3), 624–632.

647 (37) Veličković, D.; Zhang, G.; Bezbradica, D.; Bhattacharjee, A.; Paša-Tolić, L.; Sharma, K.;  
648 Alexandrov, T.; Anderton, C. R.; KPMP Consortium. Response Surface Methodology As a New  
649 Approach for Finding Optimal MALDI Matrix Spraying Parameters for Mass Spectrometry  
650 Imaging. *J. Am. Soc. Mass Spectrom.* **2020**, *31* (3), 508–516.

651 (38) Homeffer, V.; Strupat, K.; Hillenkamp, F. Localization of Noncovalent Complexes in MALDI-  
652 Preparations by CLSM. *J. Am. Soc. Mass Spectrom.* **2006**, *17* (11), 1599–1604.

653 (39) Bowman, A. P.; Blakney, G. T.; Hendrickson, C. L.; Ellis, S. R.; Heeren, R. M. A.; Smith, D. F.  
654 Ultra-High Mass Resolving Power, Mass Accuracy, and Dynamic Range MALDI Mass  
655 Spectrometry Imaging by 21-T FT-ICR MS. *Anal. Chem.* **2020**, *92* (4), 3133–3142.

656 (40) La Rocca, R.; Kune, C.; Tiquet, M.; Stuart, L.; Eppe, G.; Alexandrov, T.; De Pauw, E.; Quinton,  
657 L. Adaptive Pixel Mass Recalibration for Mass Spectrometry Imaging Based on Locally  
658 Endogenous Biological Signals. *Anal. Chem.* **2021**, *93* (8), 4066–4074.

659 (41) McCann, A.; Rappe, S.; La Rocca, R.; Tiquet, M.; Quinton, L.; Eppe, G.; Far, J.; De Pauw, E.;  
660 Kune, C. Mass Shift in Mass Spectrometry Imaging: Comprehensive Analysis and Practical  
661 Corrective Workflow. *Anal Bioanal Chem* **2021**, *413* (10), 2831–2844.

662 (42) Ge, J.; Ma, C.; Qi, Y.; Wang, X.; Wang, W.; Hu, M.; Hu, Q.; Yi, Y.; Shi, D.; Yue, F.; Li, S.;  
663 Volmer, D. A. Quadrupole Detection FT-ICR Mass Spectrometry Offers Deep Profiling of  
664 Residue Oil: A Systematic Comparison of 2ω 7 Tesla versus 15 Tesla Instruments. *Analytical  
665 Science Advances* **2021**, *2* (5–6), 272–278.

666 (43) van Agthoven, M. A.; Lam, Y. P. Y.; O'Connor, P. B.; Rolando, C.; Delsuc, M.-A. Two-  
667 Dimensional Mass Spectrometry: New Perspectives for Tandem Mass Spectrometry. *Eur  
668 Biophys J* **2019**, *48* (3), 213–229.

669